Aluminium promoted sulfidation of ammonium perrhenate: presence of nanobattery in the ReS_2 composite material based memcapacitor

Joanna Borowiec,[1,2] Weizheng Liang,[2] Filippo S. Boi,[1] Yi He,[3] Shan L. Wang,[3] William P. Gillin,[1,4]*

[1] College of Physics, Sichuan University, 610064, Chengdu, People's Republic of China

[2] The Peac Institute of Multiscale Sciences, 610031, Chengdu, People's Republic of China

[3] Analytical and Testing Center, Sichuan University, 610064, Chengdu, People's Republic of China

[4] Materials Research Institute and School of Physics and Astronomy, Queen Mary University of London, Mile End Road, London, E1 4NS, United Kingdom

*Corresponding author. Tel/Fax: +86-28-85412322. E-mail address: borowiec@scu.edu.cn (J. Borowiec)

Abstract:

This study demonstrates a new approach to the synthesis of rhenium disulfide (ReS_2) in a sulfidation reaction of ammonium perrhenate (NH_4ReO_4), occurring at room temperature and in water solution. It was found that aluminum (Al) plays a catalytic role in the reaction taking place in low ionic strength solutions. The reaction product is characterized using several analysis techniques, including energy dispersive X-ray spectroscopy (EDX), X-ray photoelectron spectroscopy (XPS), X-ray diffraction (XRD), transmission electron microscopy (TEM), Raman

spectroscopy and thermogravimetric analysis (TGA). Furthermore, an interesting observation of both memristive and memcapacitive effects, existence of nanobattery with an electromotive force estimated to be 0.80V, in a prototypical device based on the as-synthesized ReS_2 composite material is presented. This finding shows promise for the implementation of the ReS_2 in the next generation memristor technology.

Key words: rhenium disulfide, bipolar resistance switching, memcapacitor, nanobattery

1. Introduction

Rhenium disulfide (ReS_2) belongs to the class of 2 dimensional transition metal dichalcogenides (2D TMDs) [1], and is an emerging semiconductor due to its distinguishable properties in the aspect of not only its anisotropy, chemical stability, or mechanical flexibility but also the possibility to tune its properties with doping or the prospects of its integration with other 2D heterostructures for functional devices fabrication [2-6]. Accordingly, among a large number of reports concerning electronic devices based on diverse TMDs [7-9], the ReS_2 was demonstrated to have a great potential for utilization in the field effect transistors, photodetectors, digital logic, and energy storage devices [4, 10-15]. Furthermore, for the first time, an interesting effect of the negative differential resistance has been recently reported in a phosphorene/ReS_2 heterojunction based device [16]. Among them, other types of TMDs such as 1T-TaS_2, MoS_2 and n-doped MoS_2-polyvinylpyrrolidone (PVP) nanocomposite [17-21] exhibited resistance switching characteristic. Memristor principle of operation is based on the phenomenon of resistance change of the device active material, which is desirable from the perspective of their application in the emerging, next generation memory storage technology (memristor technology). In order to meet the requirements of modern electronics, only the

memristors of excellent performance and low cost of fabrication of active materials, used for their construction, can be considered for utilization in the industry [22]. A key role in the development of the high-performance memristor is the search for, design and synthesis of materials exhibiting desirable properties. However, a limited number of reports regarding resistive switching, identified in TMDs or their composites, points on the still initial stage of their implementation [17-21]. Till the present day, many of the reported devices can't meet the criteria for data storage in modern electronics. Consequently, a search for novel composite materials is necessary and of great importance to carry out further theoretical and experimental studies.

Despite a number of well explored routes leading to the synthesis of ReS_2, such as mechanical cleavage [23], liquid or chemical exfoliations [24, 25], and chemical vapour deposition (CVD) [4, 26] methods, to the best of our knowledge, there is limited number of scientific studies presenting bulk synthesis of the ReS_2 achieved *via* sulfidation processes of Re precursors. Above mentioned methods are not ideal as they either rely on complex processes requiring high vacuum and elevated temperatures, or harsh chemical reaction environment. Considering previous reports, we can see dependence, to a large degree, of the sulfidation processes of the NH_4ReO_4 or Re_2O_7 precursors on the temperature, content of water, or the necessity of a catalyst use to obtain satisfactory reaction efficiency [27-29]. For comparison, introduced here sulfidation process is not only based on the cost effective one pot synthesis, carried out from water soluble precursors taking place at room temperature and ambient pressure but also is inherently scalable. In addition, this approach extends the scope of available soft chemical synthesis methods of ReS_2 allowing its easy adaptation for large scale production.

This study demonstrates intriguing electronic properties of the fabricated device utilizing the ReS_2 based composite material, which has been synthesized using bottom-up chemical synthesis method. The synthesis leads to a product in a bulk quantity thus allows its easy integration into electronic devices *via* solution processing techniques. It was found that the room temperature sulfidation process occurs due to the catalytic properties of aluminum (Al). Most likely, it is facilitated by adsorption of ReO_4^- ions on the Al catalyst surface, for which the activation energy of the reaction is lowered as a consequence of the Re−O bonds polarization. A detailed characterization of the synthesis product has been performed using combination of spectroscopy techniques, including Raman, infrared (IR), energy dispersive X-ray (EDX), X-ray photoelectron (XPS) spectroscopy, as well as transmission electron microscopy (TEM), thermogravimetric analysis (TGA) and differential scanning calorimetry (DSC). Moreover, we provide experimental evidence of the coexistence of both resistive and capacitive effects identified in one device, based on the as-synthesized ReS_2 composite material. The preliminary electric characterization of the device was carried out, and the possible mechanisms of the observed dual resistive and capacitive memory effects were briefly presented and discussed. Those extraordinary properties of ReS_2 composite material are of great significance and interest from the research and industrial communities, due to the possibilities of its utilization in devices of novel functionalities, beyond what was accomplished up to the present moment, such as reconfiguration architectures [30], neuromorphic computing [31] and artificial synapses [32].

2. Materials and Methods

2.1. Materials

Ammonium perrhenate (NH_4ReO_4, purity ≥ 99.9%) was provided by Sigma Aldrich (Shanghai, China). Sodium sulfide nonahydrate ($Na_2S·9H_2O$, purity ≥ 98%), acetone, ethyl and isopropyl

alcohol were purchased from Keshi Chemical Company (Chengdu, China). The chemicals were used without further purification. Aluminum pellets (purity of 99.999%) were provided by Alfa Aesar.

2.2. Aluminium catalyst preparation

Aluminum film (thickness ~400 nm) was prepared by physical vapour deposition (PVD) method on a glass substrate in a vacuum chamber (Xiwoke Co., China). Prior to the experiment, the glass substrates were cleaned with ethyl and isopropyl alcohol by treatment in an ultrasonication bath for 5 min, and finally dried in a flow of high purity N_2 gas.

2.2. ReS_2 synthesis procedure

The synthesis was performed under an ambient atmosphere (temperature 22°C, humidity ~70%). First, the Al/glass substrates were cleaned three times with ethyl and isopropyl alcohol by treatment in an ultrasonication bath for 5 min, and dried in a flow of high purity N_2 gas. In separate glass vessels, the NH_4ReO_4 (0.19 mmol) and $Na_2S{\cdot}9H_2O$ (0.38 mmol) compounds were dissolved in 1.8 and 1.0 mL of water, respectively. In the next step, both solutions were mixed and directly transferred using micropipette on the Al/glass substrate. Immediately, a formation of gas bubbles and the dark brown product was observed. The reaction propagated until the Al film was completely dissolved in the highly alkaline reaction environment. Nevertheless, the reaction could be continued by transfer of the reaction mixture onto another fresh Al/glass substrate. Finally, the reaction product was purified in water using a molecular porous membrane (MWCO 8 kDa), collected by centrifugation and dried at room temperature.

2.3. ITO/ReO_3-ReS_2/Al device fabrication

First, the substrates of indium tin oxide (ITO, 200 nm) on glass were patterned using photolithography method. Prior to the device fabrication, the ITO/glass substrates were cleaned

three times in acetone, ethyl and isopropyl alcohol by treatment in an ultrasonication bath (10 min), and dried in a flow of high purity N_2 gas. The water:ethyl alcohol suspension (v/v, 1:0.1, concentration 1.7 mg/mL) of as-synthesized ReS_2 was prepared by ultrasonication (1 h), and used to form the active layer by spin coating process (500 rpm, 30 s) on the cleaned ITO/glass substrates. In the final step, the aluminum top electrode (thickness ~110 nm) was deposited by thermal evaporation in a PVD chamber, under vacuum of 10^{-4}-10^{-3} Pa.

3. Results

3.1 Compositional and structural analysis

3.1.1 EDX analysis

First of all, the compositional and elemental analyses of the synthesis product were conducted using an energy dispersive X-ray (EDX) spectroscopy method. Figure S1 of the electronic supporting information (ESI) shows the EDX results indicating the presence of rhenium (Re), sulfur (S), carbon (C) and oxygen (O) atoms in the examined sample. Based on the atomic percentages of the elements, the ratio of S and Re was estimated to be $ReS_{2.46}$. Additionally, elemental mapping and several SEM images of the synthesis product are presented in Figure S2.

3.1.2 XPS analysis

The bonding configurations of the Re and S atoms were examined by recording high-resolution 4f and 2p XPS spectra of ReS_2, respectively. After the peak deconvolution procedure, data shown in Figure 1A, we could identify two doublets located at the binding energies (BEs) of 42.38 and 44.78 eV. These BEs are characteristic for the $4f_{7/2}$ spin-orbit split doublet of Re in the Re^{4+}, corresponding to the ReS_2 [4] and in the Re^{6+} oxidation state [33], respectively. Deconvolution of the high resolution 2p spectrum of S (Figure 1B), revealed a complex environment composed of four characteristic doublets corresponding to the core $2p_{3/2}$ level peaks

of S in the form of sulfide (S^{2-}, assigned to terminal S atoms in polysulfides S_n^{2-}) located at 161.74 eV [34], disulfide (S_2^{2-}) at 162.96 eV [4], sulfinyl (SO^{2-}) [35] located at 166.29 eV and sulfate (SO_4^{2-}) at 167.98 eV [36]. We are convinced that other S containing surface bounded species, such as: sulfur (IV) oxide (SO_2) [35], methylsulfonyl (SO_2CH_3, 168.0 eV) [37], thiosulfate ($S_2O_3^{2-}$, 167.7 eV) [35], or persulfate ($S_2O_8^{2-}$, 168.10 eV) [38] might contribute to the S 2p peaks of the highest BE values. In comparison to the EDX results, the XPS analysis indicated a slightly higher ratio of Re:S estimated to be 1:2.7, which is most likely associated with an overlap of the S_2^{2-} $2p_{3/2}$ peak with the one representing central S atoms in S_n^{2-} [34]. The high resolution spectrum of carbon (C 1s, Figure S3A of the ESI), shows several peaks typical for a carbonaceous matter occurring as a surface overlayer.

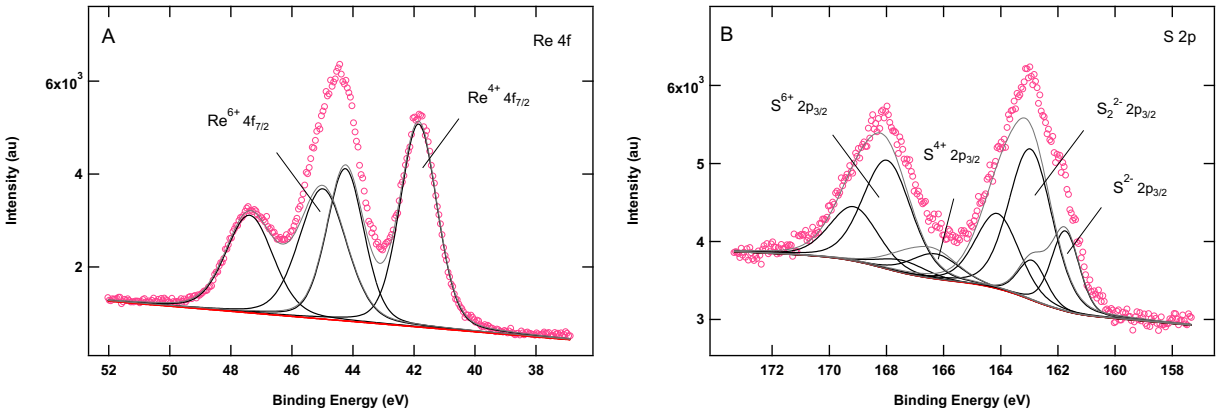

Figure 1 High resolution XPS spectra of A) Re 4f and B) S 2p, recorded at an emission angle normal to the sample surface.

For these species, the deconvolution procedure indicated emissions from various functional groups, such as adventitious carbon (C−H, C−C at 284.62eV), hydroxyl, ether or C−S group (C−OH, C−O−C at 286.54 eV), and ester or acid functional group (O−C=O at 288.48eV) [39]. Furthermore, extended delocalized electrons resulted in photoelectron plasmon loss feature peaks (π−π* transition peaks) located at 291.75 and 294.39 eV, demonstrating that the sp^2 bonds are

dominant in the surface C layer [40]. The relative peak intensity ratios were estimated to be 96.13 % (at 284.6 eV) and 3.87 % (at 285.15 eV) for sp^2 and sp^3 bonded C, respectively. Noteworthy, the π−π* transition peaks are absent in the C 1s XPS spectrum of the unpurified product (Figure S3B), indicating an occurrence of secondary reactions of the surface atoms with various water dissolved molecules (mostly CO_2 and CO). The high resolution oxygen spectrum (O 1s, Figure S3C of the ESI) demonstrates peaks corresponding to O in the form of metal oxide (O−O at 530.00 eV), hydroxyl and organic C−O groups (C−OH, C−O at 531.75 eV) as well as a carbonyl group together with surface adsorbed water (C=O, H_2O at 533.10 eV) [39]. Additionally, in the spectrum of the purified sample (Figure S4) we can observe an appearance of nitrogen (N 1s, 400.47 eV) peak (assigned to C−N bonding) [41], originating from the sample surface atoms reaction with water dissolved gaseous N_2 or nitrogen oxides.

3.1.3 XRD analysis

The XRD pattern of the as-synthesized ReS_2 with assigned major Bragg reflections is presented in Figure 2. The diffraction peak assignation is in agreement with the reference pattern of triclinic ReS_2 and fall under the space group Pī (JCPD 82-1379) [2]. The fitted peak position values are collected in Table S1 (ESI). In comparison to the reference lattice spacing [2], we can notice a slight expansion of the (100), (01-2) and (1-21) lattice planes of 0.02, 0.19 and 0.18 Å, and a contradiction of the (001) lattice plane of 0.14 Å. These observable changes in the distances between the lattice planes can be explained by taking under consideration the synthesis method, where imperfect stacking of the ReS_2 layers could result from the surface covered with a noticeable amount of diverse C species (see Figures S3A and B of the ESI) or inorganic impurities. Additionally, from the process of chemical synthesis, we can expect foreign atoms

inclusion in the lattice of the ReS_2 crystal, or stress resulting from the deformation of ReS_2 layers [42, 43].

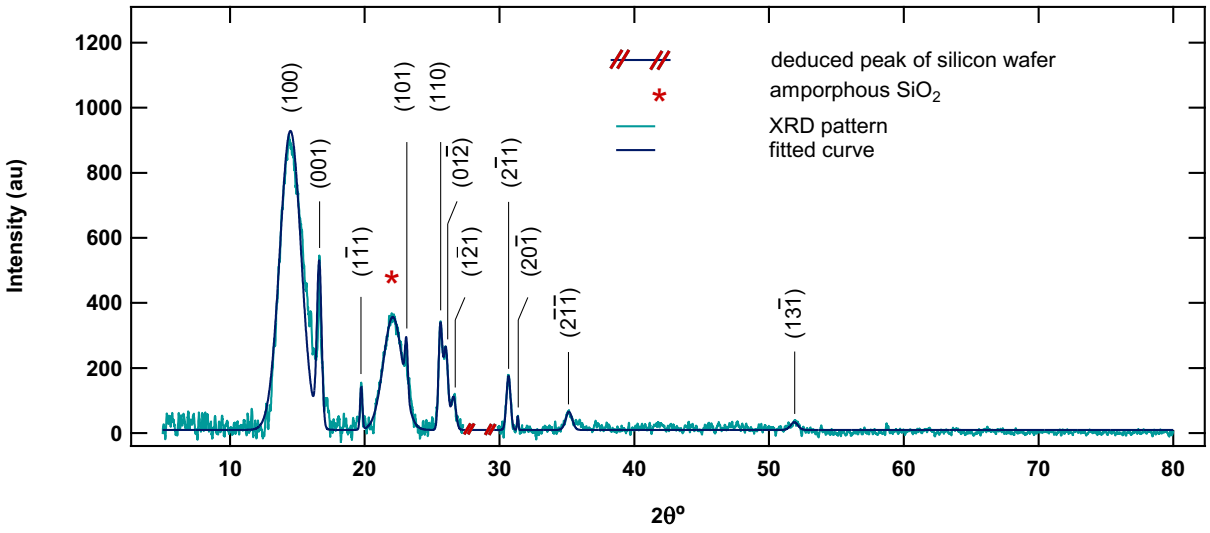

Figure 2 XRD pattern of ReS_2 with assigned crystallographic indices.

3.1.4 TEM analysis

Supporting the XRD results, several TEM images of ReS_2 have been acquired as shown in Figure 3. Figure 3C-F present high resolution TEM (HR TEM) images, taken from the areas indicated by squares (labeled in Figure 2B from 1 to 4), with the corresponding images from the Fast Fourier Transform (FFT) analysis [Insets 1-4, Figure 3C-F] of the ReS_2 crystal. The diffraction spots were assigned to (100), (010) [Figure 3C] and (200), (010) [(Figure 3D-F] planes of reflection confirming crystalline nature of the product.

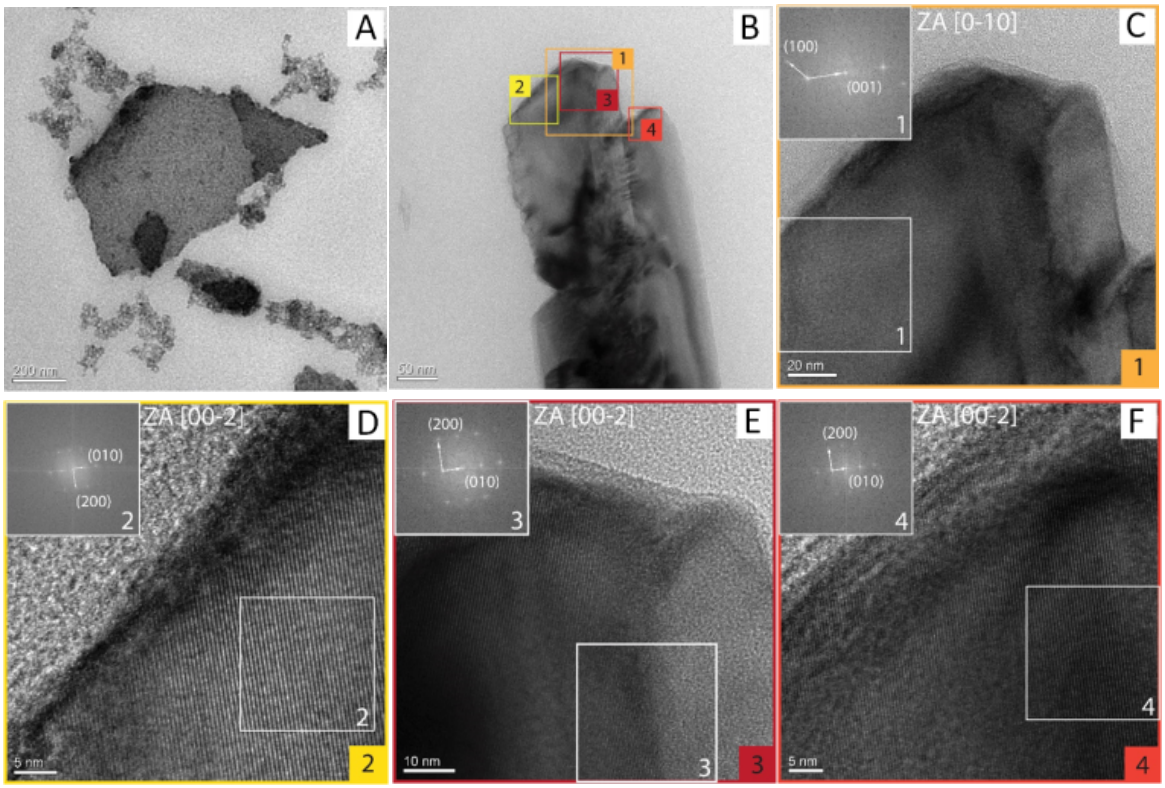

Figure 3. A-F) TEM images of ReS_2; and G-J) HR TEM images of ReS_2 acquired from areas 1-4, indicated by squares in (F) and centered at the [0-10] (G) and [00-2] (H-J) zone axis. Insets: Images of FFT analysis acquired from areas 1-4.

3.1.5 Raman spectroscopy analysis

An undistorted tetrahedral (T_d point group symmetry) ReO_4 molecule exhibits four fundamental Raman modes [44]. However, the symmetry of T_d coordinated ReO_4^- molecules confined to a crystalline lattice is lower than T_d, due to molecule distortions arising from the need of its accommodation to the lattice structure. The distortions cause a shift of the bands frequency values, as well as a split of the band representing bending modes. Due to the aforementioned, in the case of NH_4ReO_4/Al (Figure 4A curve (a)), we can observe lower symmetry surface coordinated ReO_4^- molecules and in effect more complicated Raman spectrum.

Based on the reference frequency values, we could assign the bands to the Re=O symmetric stretching mode at 967.85 ± 0.02 cm^{-1}, antisymmetric stretching mode that splits into two peaks at 915.73 ± 0.13 and 893.28 ± 0.13 cm^{-1}, as well as to the lifted degeneracy of the Re–O bending mode giving rise to bands at 343.09 ± 0.17, 335.23 ± 0.31 and 328.49 ± 0.45 cm^{-1} [44, 45].

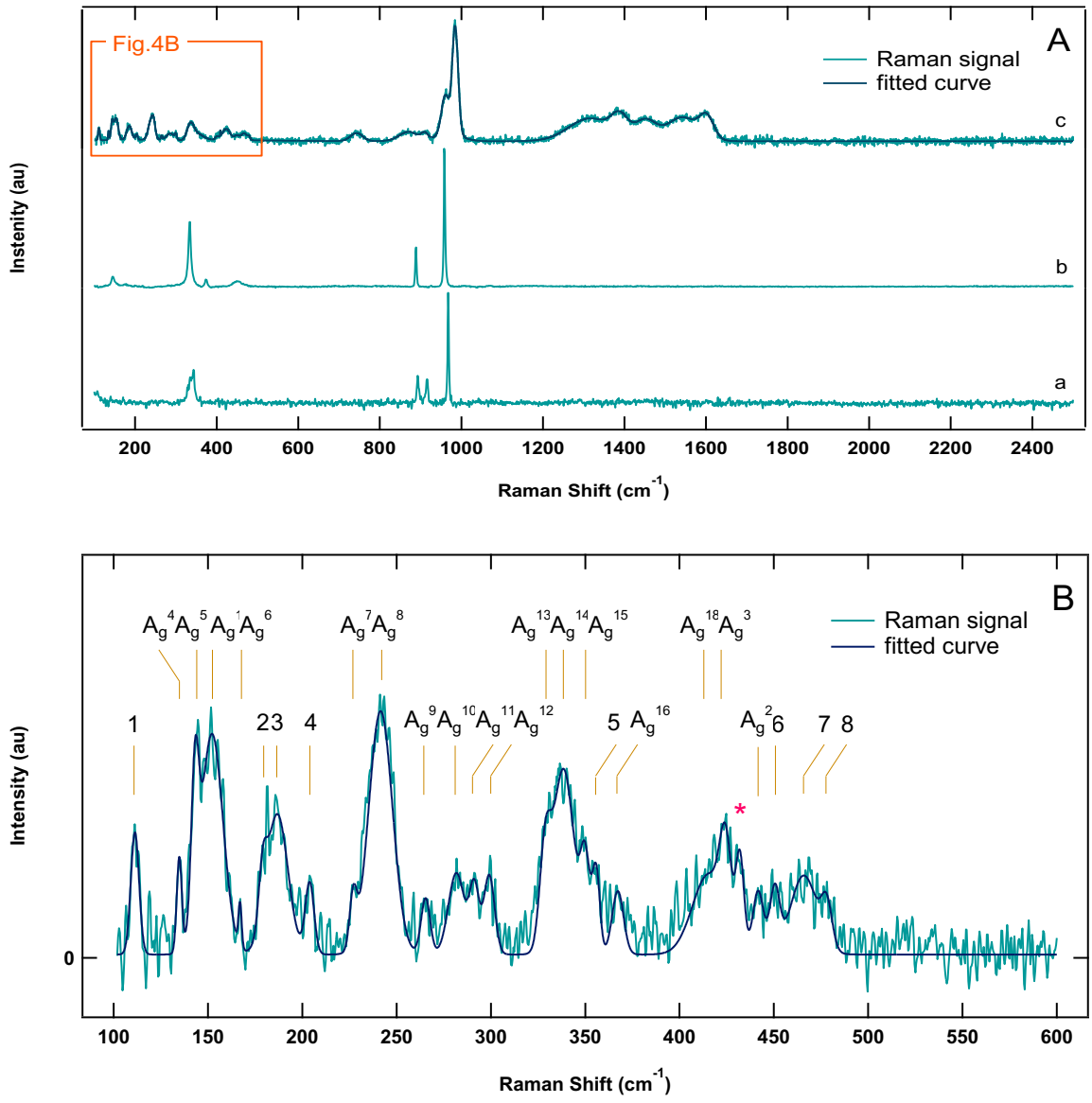

Figure 4 A) Raman spectrum recorded at ambient conditions for curve: a) NH_4ReO_4/Al, b) synthesis product before purification, and c) purified product; B) low frequency Raman spectrum of the purified product.

In the case of the Raman spectrum recorded for the synthesis product before purification (Figure 4A curve (b)), we can notice not only a significant change in the relative intensities of the bands in a high frequency region but also slight shift in their frequencies of antisymmetric (888.57 ± 0.05 and 925.80 ± 1.59 cm^{-1}) and symmetric (958.56 ± 0.01 cm^{-1}) stretching modes of the Re–O in ReO_4^- molecules, indicating change in their symmetry. In addition to the lower frequency bending modes at 333.8 ± 0.05 and 373.99 ± 0.33 cm^{-1}, we notice newly appeared lattice vibration modes at 145.9 ± 0.35 and 176.01 ± 0.76 cm^{-1} [44, 45]. Taking under account the composition of the examined sample, the weak peak at 176.01 ± 0.76 cm^{-1} might indicate presence of the Re–O–Re linkages [44], and together with the broadened peak, centred at 451.51 ± 0.93 cm^{-1} (composed of overlapped peaks between 436.06 and 476.05 cm^{-1}), at the same time it can be related to the S−S stretching and lattice modes of the S_2^{2-} anion or higher polysulfide anions (S_n^{2-}), respectively [46]. We also observe peaks at 145.9 ± 0.35 and 218.28 ± 1.23 cm^{-1} associated with the Re in-plane vibrations in ReS_2 [47].

An observable change in the Raman spectrum recorded for the purified product can be seen in Figure 4A curve (c). Most importantly, the bands between 888.57 and 958.56 cm^{-1} (present in Figure 4A curves (a) and (b)) were replaced by two broad bands centred at 742.93 ± 0.60, 870.54 ± 1.08 and 909.93 ± 0.71 cm^{-1}, which could be ascribed to the Re−O stretching modes similar to those observed in low symmetry rhenium (VI) oxide (ReO_3) [48, 49], but at the same time the peak at 870.54 ± 1.08 cm^{-1} might represent the vibrations of the Re−O−Re linkages (ReO_3−O−ReO_3 in Re_2O_7), accompanied by overlapped and broadened bands at ~465 and ~180 cm^{-1} (bands 2-4 and 6-8, Figure 4B) [44]. The lowest frequency band (indicated as 1, Figure 4B) most probably corresponds to the lattice vibrations of ReO_4^- [45]. The higher intensity narrow bands at 960.53 ± 0.17 and 984.87 ± 0.06 cm^{-1} originate from the symmetric Re=O bond

stretching vibrations [50]. It is worth to mention, that bands located at ~240, 350, 470, 750, 885 and 992 cm^{-1} have been also identified in the ReO_3 films deposited by evaporation in the reducing environment [51]. The ambiguity of the bands assignment should be interpreted not only based on the existence of the Re−O bonding in diverse configuration but also complex coordination geometry of the molecules.

Interestingly, the Raman spectrum of the purified sample shows characteristic pattern exhibiting broadened and overlapped peaks centered at 1380.30 ± 0.75 and 1575.10 ± 0.47 cm^{-1} (for details on the bands location see Table S2, ESI), featuring the D and G bands of C characteristic for all poly-aromatic hydrocarbons [52]. The main G band represents in-plane sp^2 C–C stretching mode (in both rings and chains) [53] and appears for all sp^2 C systems, including amorphous carbon, carbon nanotubes, and graphite, with the alteration of the line shape depending on the material quality [54]. The D band is due to the breathing modes of sp^2 C atoms in rings attributed to the presence of structural defects [52, 53, 55]. Raman spectra of C films are dominated by the sp^2 C sites, as a result of a visible excitation that always resonates with the π states. For this reason, even for a substantial amount of amorphous sp^3 C the visible Raman analysis portrays sp^2 vibrations. The ReS_2 surface coverage with diverse compounds (see XPS analysis for details), led in some cases to the significant broadening and overlapping of Raman bands at low frequencies. Nonetheless, low frequency peaks corresponding to the ReS_2 have been identified by carrying multiple peak fitting procedure of the acquired spectrum. The result is presented in Figure 4B, with the corresponding fitted frequency values collected in Table S2 (ESI).

The Raman peaks indexing of the ReS_2 (Figure 4B) has been borrowed from McCreary et al. [47]. Accordingly, the A_g^1 corresponds to a single in-plane mode of the ReS_2 with all vibrations

parallel to the plane, the out-of-plane S atoms vibrations are represented by the A_g^2, and quasi-out-of-plane vibrations of S atoms, at slight angles with respect to the basal plane, are indicated by the A_g^3 mode. Other identified modes can be ascribed to the vibrations of atoms at varying angles as a consequence of lower crystal symmetry of the ReS_2. The low frequency A_g^4 mode represents predominately Re out-of-plane vibrations, Re in-plane vibrations are assigned as the A_g^1, A_g^6, A_g^7, and A_g^8. Finally, the S vibrations in the ReS_2 are indicated as the A_g^2, A_g^3, and modes from A_g^9 to A_g^{18} [47]. The frequency distributions of the assigned modes are in agreement with those obtained in earlier studies [47, 56]. Nonetheless, slight shifts of the peak frequencies can be explained considering the synthesis method, where various surface molecules and impurities may influence the frequencies of atoms vibrations.

3.1.6 IR spectroscopy analysis

The mid-infrared spectrum is presented in Figure 5. Correspondingly, the first weak band at 3739.89 cm^{-1} is related to the H_2O vibration modes [57], meanwhile, the broad peak centered at 3411.11 cm^{-1} indicates the presence of exchangeable protons, typically from the H_2O (symmetric and antisymmetric stretching), alcohol or carboxylic acid groups [58].

A lower frequency band originating from the O–H bending modes of the H_2O molecules incorporated between the lattice planes of the ReS_2 crystal appears at 1619.81 cm^{-1} [59], and might overlap with the C=C stretching (alkene or aliphatic molecules) band. Alkane C–H bending mode of methyl ($–CH_3$) group exhibits an *umbrella mode* at 1379.65 cm^{-1} [58]. We can also identify the very weak contribution from the carbonyl group (C=O) vibrations in ketone or ester at the frequency of 1735.69 cm^{-1} [58]. The peak linked with the S=O stretching vibrations in sulfate can be found between 1450 and 1350 cm^{-1}, meanwhile, the SO_2 group asymmetric

stretch and the S=O stretch of sulfur compounds give rise to the bands in the range of 1190-1120 cm^{-1} and 1060-1020 cm^{-1}, respectively [58, 60].

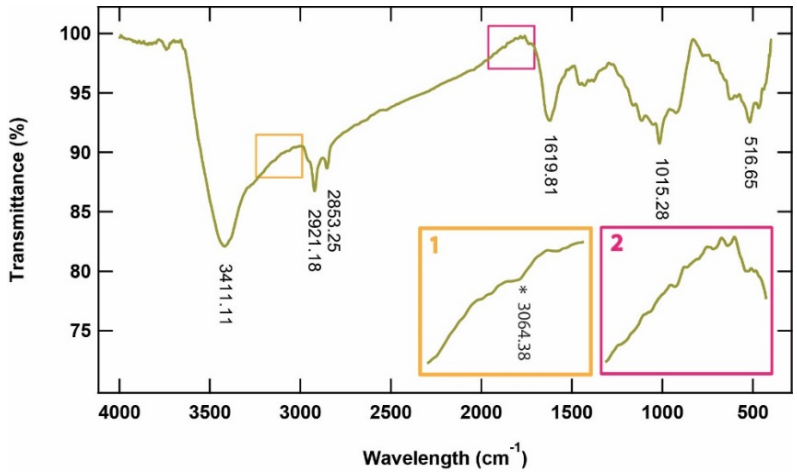

Figure 5 Infrared spectrum recorded at room temperature under ambient atmosphere.

The peak related to the CH_2 wagging can be seen at the frequency of 1159.96 cm^{-1}, and the one of the C–O stretching vibration at 1015.28 cm^{-1} [58]. The C–S and S–S disulfide stretching vibrations have been assigned to the bands in the region of 700.65-516.65 cm^{-1} and 516.65-441.09 cm^{-1} [60]. The peak at 924.48 cm^{-1} is related to stretching vibrations of the H–C–S group or sulfonic acid (HSO_3^-) [60], and the peak at 774.31 cm^{-1} to the S–OR in ester. The former band with the one at 625.50 cm^{-1} might also be attributed to the C–S stretching vibrations [58, 60]. Referring to the results from the C 1s XPS (Figure S3A) and Raman (Figure 4A curve (c)) spectra, where a clear demonstration of the sp^2 bonded C species has been shown, we can assign several weak bands to the aromatic groups. Accordingly, graphitic-like species present on the sample surface gave rise to a very weak peak at 3064.38 cm^{-1} (Inset 1, Figure 5), the bands between 2000-1700 cm^{-1} (Inset 2, Figure 5) as well as the one in the range from 1454.29 to 1431.04 cm^{-1}, which can be ascribed to the C–H stretching, to the combination and overtone bands and to the C=C stretching modes, respectively. Finally, referring to the inorganic groups

that were determined by the XPS method, we can assign the bands appearing between 1130-1080 cm^{-1} and 680-610 cm^{-1} to the sulfate (SO_4^{2-}) group vibrations [58].

3.1.7 Thermogravimetric analysis

The thermogravimetry (TGA) and differential thermogravimetry (DTG) analyses, spectra are shown in Figure 6A and B, revealed three major steps of the product decomposition. In the first step, from 30°C to about 600°C the weight decrease by 26.30 % is mainly due to the processes of adsorbed water loss, gaseous residues (such as CO, CO_2) from the most labile carboxylate and anhydride functional groups loss (150-300°C) together with removal of the more stable oxygen groups, such as phenol and carbonyl (300-500°C). In the second step, at temperatures above 600°C, we can observe a slight increase in the rate of the sample decomposition up to 950°C, with a weight loss of 21.96%. Due to our considerations, this step can be associated with desorption and disproportionation of variously surface bonded Re^{6+} in the form of oxide [61, 62] (see discussion below).

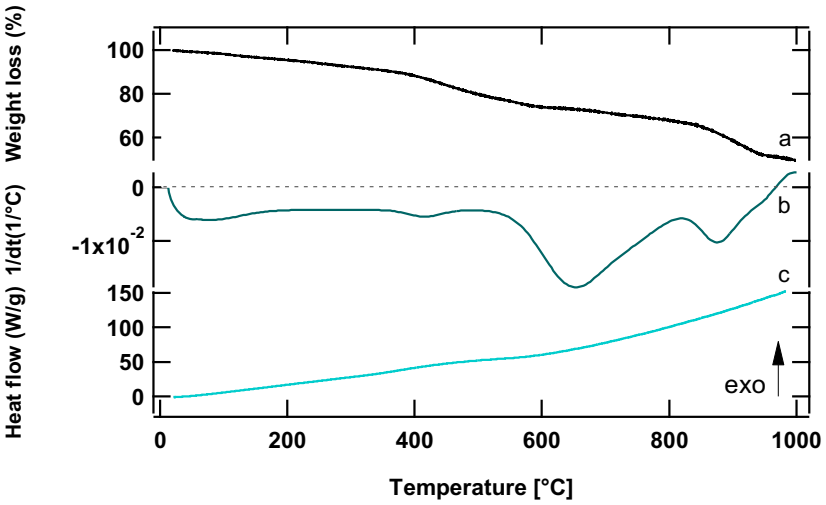

Figure 6 Spectrum of (a) TGA, (b) DTG and (c) DSC of as-synthesized ReS_2 carried out under inert atmosphere.

The third and the final step is associated with the weight decrease of 8.16%, from 810 up to 1000°C and is most likely related to the evaporation of the inorganic sulfate (SO_4^{2-}) [63], as well as to the decomposition of the ReO_2, if present ($7ReO_{2(s)} \rightarrow 3Re^0 + 2Re_2O_{7(g)}$) [61, 64]. As it is presented in the differential scanning calorimetry (DSC) profile (Figure 6C), the exothermic characteristic points out on secondary processes taking place in the studied system, which are most likely related to the recrystallization and/or surface reconstruction of the sample upon thermal treatment.

3.2 Electrical characterization of the ITO/ReO_3-ReS_2/Al memcapacitor

The preliminary study of the electrical properties of the synthesized composite material based on the ReS_2 (ReO_3-ReS_2) were conducted in a device comprised of the active material, sandwiched between the bottom (BE, indium tin oxide (ITO)) and top (TE, aluminum (Al)) electrodes. Interestingly, as presented in Figure 7 the ITO/ReO_3-ReS_2/Al device in contrast to the ideal memristor [65], possesses a non-zero current-voltage (*I*-*V*) crossing characteristic (point A in Figure 7), indicating coexistence of the two dynamic elements, namely resistance (memristance, R_m) and negative capacitance (memcapacitance, C_m) in one device [66, 67].

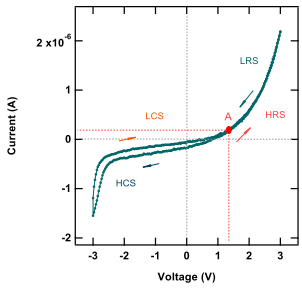

Figure 7 The *I-V* plot of the ITO/ReO_3-ReS_2/Al memcapacitor. Arrows indicate potential sweep direction. Sweep voltage range: ±3V, compliance current (I_{cc}): 1 mA, and frequency: 10Hz.

As it is demonstrated in Figure 7, the device operates in bipolar mode, switching from a high resistance state (HRS) to a low resistance state (LRS), and subsequently from a high capacitive state (HCS) to a low capacitive state (LCS). The existence of the dynamic effect can be evidenced by the significant dependence of the device resistive and capacitive states on the scan frequency (ω).

As is depicted in Figure 8, at low frequencies (ω= 10 Hz) both the memristive and memcapacitive states are observed. The non-zero crossing point of the bipolar switching was determined to take place at the voltage of 1.3V corresponding to the current value of 1.7×10^{-7}A. What is more, the appearance of the electromotive force (*emf*) of 0.80V proves the existence of the nanobattery within the device active layer [68]. However, under an increase of the scan frequency ($\omega\geq$ 100Hz) a substantial change in the ITO/ReO_3-ReS_2/Al hysteresis is evidenced,

where the memristive signature completely disappears giving rise to a square-like loop featuring an entirely memcapacitive device behaviour.

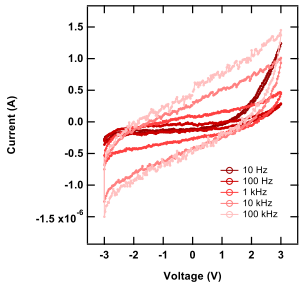

Figure 8 The *I-V* dependence on the scan frequency of the ITO/ReO_3-ReS_2/Al memcapacitor. Sweep voltage range: ±3V, and compliance current (I_{cc}): 1 mA.

A contribution of the parasitic effect into the capacitance under the subsequent increase of the scan frequency results in a significant current instability, clearly noticeable in the case of voltage sweep at frequencies of 10 and 100 kHz (Figure 8). The increase of the frequency and in the effect an electric field (*EF*) within the active material alters both the faradaic and non-faradaic processes. A transition from the memristive and memcapacitive to the purely memcapacitive state of the ITO/ReO_3-ReS_2/Al device can be understood from the perspective of a physical transition from the ions migration within the composite layer, at slow bias sweep, to its static accumulation at very high scan frequencies. As it is expected, an apparent capacitance (C_{app}) decreases with the increase of the scan frequency (data plot shown in Figure S7A and B) due to the limited diffusion of the ions, altering their effective interactions with the active electrode.

The numerical values of C_{app} computed for bias sweep at various scan frequencies are collected in Table S3.

4. Discussion

In this study, we demonstrate a simplistic reaction between the mixture of the NH_4ReO_4 and $Na_2S{\cdot}9H_2O$ occurring at room temperature, and most importantly in water solution. For this process, noncatalytic route is unsuccessful at room temperature, and the sulfidation reaction is initiated only in the presence of the Al catalyst. In the solutions of high pH value, the perrhenate ion exists as the ReO_4^- [69], meanwhile, the Na_2S dissociates to form S^{2-} and HS^- ions [70]. The adsorption of the ReO_4^- ions takes place immediately after contact of the reaction mixture with the Al catalyst surface, wherefore the sulfidation is instantly initiated. Most likely, the steric effect resulting from the change of the adsorbed ReO_4^- molecules symmetry (see Figure 4) causes the Re−O bonds polarization, which in consequence lowers the activation energy of the sulfidation process. Nonetheless, the Al catalyst role of providing an alternative mechanism of the sulfidation reaction can't be entirely ruled out. As the reaction propagates, the Al catalyst film undergoes dissolution in highly alkaline environment, following the reaction: $2Al^0 + 2OH^- + 6H_2O \rightarrow 2[Al(OH)_4]^- + 3H_{2(g)}$, to form tetrahydroxoaluminate complex ion, which exist in a solution as the $Al(OH)_4^-$ or either $[Al(H_2O)_2(OH)_4]^-$ ions. After complete dissolution of the Al film, a creation of a thin layer of the product (also present in a water dispersed form) adhered to the surface of the glass substrate can be observed, along with a bubble like structures originating from the $H_{2(g)}$ and partial $NH_{3(g)}$ evolution (Figure S6). In the additional experiment, we have replaced the Al catalyst with γ-aluminum (III) oxide (γ-Al_2O_3), however, in contrast to other reports, no catalytic effect of the γ-Al_2O_3 has been found [27].

The sulfidation reaction is promoted by Al towards ReS_2 rich in the Re^{6+} surface states, pointing out on its slightly lower selectivity toward ReS_2 formation (Figure 1A). A similar phenomenon is observed in the case of S for which a noticeable amount of S^{6+} can be seen in the XPS spectrum (Figure 1B). In addition to that, high reactivity of the product surface atoms can be observed by growth of various C rich surface species, with a perceptible amount of C in the sp^2 hybridisation (Figures S3A and B). Referring to the XPS analysis results (for the product before Figure 1A and after purification Figure S5A), we can distinguish a change in the surface bonding of the Re atoms by a shift of their formal oxidation state, where disappearance of the Re^{7+} (ReO_4^-) and subsequent increase of the Re^{6+} 4f photoelectron peaks is clearly demonstrated. This alteration is most likely attributable to the reduction processes of the Re^{7+} or change in the ReO_4^- group symmetry upon its interaction with surface atoms [51]. Accordingly, several bands present in the Raman spectrum (Figure 4A curve (c)), have been previously identified as bending modes of the O−Re−O linkages in the Re^{6+} oxide (ReO_3) as well as lower crystal symmetry ReO_3 [45, 46]. Moreover, earlier studies have shown a strong reactivity of the ReO_3 surface towards the dissociation of atmospheric compounds, such as CO_2 and H_2O [49, 55, 62]. Its reactivity could explain surface alteration, through the occurrence of the secondary reactions with gaseous molecules dissolved in water, taking place during the sample purification process.

The aforementioned is evinced in the emergence of the extended delocalized electrons peak in the C 1s XPS spectrum (Figure S3A) as well as carbon D and G bands in the Raman spectrum (Figure 4A curve (c)). Referring to the latter, the ReO_4^- and ReO_3 are highly soluble in water and the observable disappearance of the Re^{7+} and presence of the Re^{6+} 4f photoelectron peaks (XPS spectra Figures S5A and 1A, respectively) confirms the existence of Re^{6+} in a form of surface bonded molecules. The change of the Re^{7+} to Re^{6+} coordination, thus in effect molecule

symmetry, can be understood not only from the shift of the highest frequency Raman peaks but also from the more complicated spectrum of the fundamental Raman bands for which splitting, broadening and overlap is evidenced. These transitions result from the complex environment of the Re^{6+}, presumably a combination of surface bonded ReO_4^-, ReO_3, Re_2O_7 and possibly other, implying uncertain bands designation which remains open to discussion and further interpretation [44, 49, 50, 62, 71].

Taking under consideration the experimental results, the resistance switching of the ITO/ReO_3-ReS_2/Al memcapacitor is postulated to be governed by geometrical (redox reactions: electrochemical metallization (ECM) process) or permittivity (permittivity switching, ionic doping) related mechanism. In principle, the ECM occurs in the devices where the electrochemically active electrode ions contribute to the conducting filaments (CFs) formation [72, 73]. The Al electrode electrochemical activity should be also accounted while considering the physical principles of operation of the ITO/ReO_3-ReS_2/Al memcapacitor. The application of the positive bias voltage to the active electrode might induce its anodic dissolution, field-driven migration of the cations in the ion conductive phase towards BE, and finally their reduction at the inert ITO counter electrode surface. The following electro-crystallization process leads to the growth of the CFs in the direction of the TE, hence switching the device into the LRS owing to the facilitated charge conduction within the developed CFs. This mechanism was identified in the mixed electronic and ionic conductivity materials, usually utilizing either Ag or Cu as the active electrode [74, 75]. However, in the ITO/ReO_3-ReS_2/Al memcapacitor, the high resistance ON state (R_{ON} ~1.38 MΩ, Figure 7) might indicate the formation of CFs without a galvanic contact with the active electrode (Al TE). This explanation is further supported by the lack of the observation of the ohmic charge carrier conduction under positive bias voltage scan (derived

from log J vs. log V plot, data not shown here), representing charge carrier conduction through formed CFs (the $J \propto V^n$ relation fitted slope values, n, were found to be <0.1). In effect, the possible charge conduction from the tip of the CF towards TE would have to be governed by the quantum mechanical tunneling.

Another possible explanation of the memcapacitor operation could be related to the polarization effect, in which the redistribution of the charges within the internal layer gives rise to an internal *EF* that opposes the external *EF* of the charged plates. This internal electric field may over screen the external field, resulting in a negative capacitance observed in the studied device [76, 77]. Moreover, as a support to the above mentioned, the existence of the nanobattery *(emf*) is observed due to the instance of the charge separation within the active material. Synthesized in this study composite material (for details please refer to the EDX and XPS results) possesses inhomogeneous phase distribution, comprised of the crystalline grains surrounded by the grain boundaries of complex chemical composition. These phases are expected to exhibit, to the certain extent, apart from electronic also ionic conduction. It is worth to mention, that in addition to the unique combination of memristor and memcapacitor, presented here device also manifests self-rectification. Presented in this study memcapacitor can be relatively easy fabricated, however in order to achieve a wide range of capacitances a full understanding of the fundamentals of the ITO/ReO_3-ReS_2/Al device operation is essential, particularly from the perspective of the dynamic changes taking place in its active layer, thus more comprehensive studies are indispensable.

5. Conclusion

In summary, this study presents the room temperature sulfidation process of the NH_4ReO_4 carried out by the $Na_2S{\cdot}9H_2O$. It has been shown, that the reaction takes place in a water solution

due to the catalytic role of the Al, and leads to the creation of ReS_2 rich in the surface Re^{6+}, S^{6+}, and sp^2 C states. The wet chemical synthesis is easily scalable and most importantly presents a new approach towards bottom up synthesis of the ReS_2 based composite material. Moreover, a demonstration of the unique combination of memristor and memcapacitor in the fabricated ITO/ReO_3-ReS_2/Al device indicates that the active material holds promise for its application in the emerging field of memristor technology.

Acknowledgment

This work was supported by the National Natural Science Foundation of China (Grant No. 61574095) and Sichuan University Full-time Post-doctoral Research and Development Fund (Grant No. 2019SCU12070). J. Borowiec and co-authors are grateful to Prof. S. N. Luo at the Peac Institute of Multiscale Sciences, for his support and for providing access to the materials characterization facilities.

Appendix A. Electronic Supporting Information

Information regarding the results and discussion of SEM, XPS, X-ray diffraction pattern data analysis, fitted Raman modes frequencies, and capacitance dependence on the scan frequency of the memcapacitor are presented in the electronic supporting information.

Declaration of Competing of Interest

The authors claim no competing of interest.

References

[1] J.A. Wilson, and A.D. Yoffe, The transition metal dichalcogenides discussion and interpretation of the observed optical, electrical and structural properties, Adv. Phys. 18 (1969) 193-335

[2] H.H. Murray, S.P. Kelty, R.R. Chianelli, C.S. Day, Structure of rhenium disulfide, Inorg. Chem. 33 (1994) 4418-4420

[3] N.R. Pradhan, et al., Metal to insulator quantum-phase transition in few-layered ReS_2, Nano Lett. 15 (2015) 8377-8384

[4] Y. Kim, B. Kang, Y. Choi, J.H. Cho, C. Lee, Direct synthesis of large-area continuous ReS_2 films on a flexible glass at low temperature, 2D Mat. 4 (2017) 025057

[5] M. Rahman, K. Davey, S.Z. Qiao, Advent of 2D rhenium disulfide (ReS_2): Fundamentals to applications, Adv. Funct. Mater. 27 (2017) 1606129

[6] F. Qi, Y. Chen, B.J. Zheng, J.R. He, Q. Li, X.Q. Wang, J. Lin, J.H. Zhou, B. Yu, P.J. Li, W. Zhang, Hierarchical architecture of ReS_2/rGO composites with enhanced electrochemical properties for lithium-ion batteries, Appl. Surf. Sci. 413 (2017) 123-128

[7] J. He, P. Li, W. Lv, K. Wen, Y.Chen, W. Zhang, Y. Li, W. Qin, W. He, Three-dimensional hierarchically structured aerogels constructed with layered MoS_2/graphene nanosheets as free-standing anodes for high-performance lithium ion batteries, Electrochim. Acta 215 (2016) 12-18

[8] M. Wu, J. Yang, D.H.L. Ng, and J. Ma, Rhenium Diselenide Anchored on Reduced Graphene Oxide as Anode with Cyclic Stability for Potassium-Ion Battery, Phys. Status Solidi RRL 13 (2019) 1900329

[9] J. He, Y. Chen, P. Li, F. Fu, Z. Wang, W. Zhang, Self-assembled CoS_2 nanoparticles wrapped by CoS_2-quantum-dotsanchored graphene nanosheets as superior-capability anode for lithium-ion batteries, Electrochim. Acta 182 (2015) 424-429

[10] E. Liu, *et al.,* Integrated digital inverters based on two-dimensional anisotropic ReS_2 field-effect transistors, Nat. Commun. 6 (2015) 6991

[11] Q. Zhang, *et al.,* Extremely weak van der Walls coupling in vertical ReS_2 nanowalls for high-current-density lithium-ion batteries, Adv. Mat. 28 (2016) 2616-2623

[12] M. Najmzadeh, C.H. Ko, K.D. Wu, S. Tongay, J.Q. Wu, Multilayer ReS_2 lateral p-n homojunction for photoemission and photodetection, Appl. Phys. Express 9 (2016) 055201

[13] F. Qi, J. He, Y. Chen, B. Zheng, Q. Li, X. Wang, B. Yu, J. Lin, J. Zhou, P. Li, W. Zhang, Y. Li, Few-layered ReS_2 nanosheets grown on carbon nanotubes: A highly efficient anode for high-performance lithium-ion batteries, Chem. Eng. J. 315 (2017) 10-17

[14] X. Xie, M. Mao, S. Qia, J. Ma, ReS_2-Based electrode materials for alkali-metal ion batteries, Cryst. Eng. Comm. 21 (2019) 3755-3769

[15] F. Qi, Y. Chen, B. Zheng, J. He, Q. Li, X. Wang, B. Yu, J. Lin, J. Zhou, P. Li, W. Zhang, 3D chrysanthemum-like ReS_2 microspheres composed of curly few-layered nanosheets with enhanced electrochemical properties for lithium-ion batteries, J. Mater. Sci. 52 (2017) 3622-3629

[16] J. Shim, *et al.,* Phosphorene/rhenium disulfide heterojunction-based negative differential resistance device for multi-valued logic, Nat. Comm. 7 (2016) 13413

[17] M. Yoshida, R. Suzuki, Y. Zhang, M. Nakano, Y. Iwasa, Memristive phase switching in two-dimensional 1T-TaS_2 crystals, Sci. Adv. 1 (2015) e1500

[18] P. Cheng, K. Sun, Y.H. Hu, Memristive behavior and ideal memristor of 1T phase MoS_2 nanosheets, Nano Lett. 16 (2016) 572-576

[19] V.K. Sangwan, D. Jariwala, I.S. Kim, K.S. Chen, T.J. Marks, L.J. Lauhon, M.C. Hersam, Gate-tunable memristive phenomena mediated by grain boundaries in single-layer MoS_2, Nat. Nanotechnol. 10 (2015) 403-406

[20] Son, D., *et al.*, Colloidal synthesis of uniform-sized molybdenum disulfide nanosheets for wafer-scale flexible nonvolatile memory, Adv. Mater. 28 (2016) 9326-9332

[21] Z. Wu, T. Wang, C. Sun, P. Liu, B. Xia, J. Zhang, Y. Liu, D. Gao, Resistive switching effect of N-doped MoS_2-PVP nanocomposites films for nonvolatile memory devices, AIP Advances 7 (2017) 125213

[22] S.J. Campbell, Is There an Immortal Memory?, Science 304 (2004) 62-63

[23] H. Jang, C.R. Ryder, J.D. Wood, M.C. Hersam, D.G. Cahill, 3D Anisotropic thermal conductivity of exfoliated rhenium disulfide, Adv. Mater. 29 (2017) 1700650

[24] J. Kang, V.K. Sangwan, J.D. Wood, X. Liu, I. Balla, D. Lam, M.C. Hersam, Layer-by-layer sorting of rhenium disulfide via high-density isopycnic density gradient centrifugation, Nano Lett. 16 (2016) 7216-7223

[25] T. Fujita, Y. Ito, Y. Tan, H. Yamaguchi, D. Hojo, A. Hirata, D. Voiry, M. Chhowalla, M. Chen, Chemically exfoliated ReS_2 nanosheets, Nanoscale 6 (2014) 12458-12462

[26] K. Keyshar, *et al.,* Chemical vapour deposition of monolayer rhenium disulphide (ReS_2), Adv. Mater. 27 (2015) 4640-4648

[27] P. Arnoldy, J.A.M. van den Heijkant, V.H.J. de Beer, J.A. Moulijn, Temperature-programmed sulfiding of Re_2O_7/Al_2O_3 catalysts, Appl. Catal. 23 (1986) 81-99

[28] J.A. Aliaga, G. Alonso-Nunez, T. Zepeda, J.F. Araya, P.F. Rubio, Z. Bedolla-Valdez, F. Paraguay-Delgado, M. Farias, S. Fuentes, G. Gonzalez, Synthesis of highly destacked ReS_2 layers embedded in amorphous carbon from a metal-organic precursor, J. Non-Cryst. Solids 447 (2016) 29-34

[29] J. Borowiec, W.P. Gillin, M.A.C. Willis, F.S. Boi, Y. He, J.Q. Wen, S.L. Wang, L. Schulz, Room temperature synthesis of ReS_2 through aqueous perrhenate sulfidation, J. Phys.: Condens. Matter. 30 (2018) 055702

[30] S. Kaeriyama, T. Sakamoto, H. Sunamura, M. Mizuno, H. Kawaura, T. Hasegawa, K. Terabe, T. Nakayama, M. Aono, A nonvolatile programmable solid-electrolyte nanometer switch, IEEE J. Solid-State Circuits 40 (2005) 168-176

[31] I. Boybat, M. Le Gallo, S.R. Nandakumar, T. Moraitis, T. Parnell, T. Tuma, B. Rajendran, Y. Leblebici, A. Sebastian, E. Eleftheriou, Neuromorphic computing with multi-memristive synapses, Nature Comm. 9 (2018) 2514

[32] J. Zhu, Y. Yang, R. Jia, Z. Liang, W. Zhu, Z. U. Rehman, L. Bao, X. Zhang, Y. Cai, L. Song, R. Huang, Ion Gated Synaptic Transistors Based on 2D van der Waals Crystals with Tunable Diffusive Dynamics, Adv. Mat. 30 (2018) 1800195

[33] M. Komiyama, Y. Ogino, Y. Akai and M.J. Goto, X-ray photoelectron spectroscopic studies of unsupported and supported rhenium using argon-ion bombardment, J. Chem. Soc. Faraday Trans. II. 79 (1983) 1719-1728

[34] M. Fantauzzi, B. Elsener, D. Atzei, A. Rigoldi, A. Rossi, Exploiting XPS for the identification of sulfides and polysulfides, RSC Adv. 5 (2015) 75953-75963

[35] B.J. Lindberg, K. Hamrin, G. Johansson, U. Gelius, A. Fahlmann, C. Nordling, K. Siegbahn, Molecular spectroscopy by means of ESCA II. Sulfur compounds. Correlation of electron binding energy with structure, Phys. Scripta. 1 (1970) 286-298

[36] W.E. Swartz, K.J. Wynne, D.M. Hercules, X-ray photoelectron spectroscopic investigation of Group VIA elements, Anal. Chem. 43 (1971) 1884-1887

[37] C.E. Mixan, J.B. Lambert, ESCA [x-ray photoelectron spectroscopic] study of the sulfur-nitrogen bond in sulfimides, J. Org. Chem. 38 **(**1973) 1350-1353

[38] X.R. Yu, F. Liu, Z.Y. Wang and Y.J. Chen, Auger parameters for sulfur-containing compounds using a mixed aluminum-silver excitation source, Electron Spectrosc. Relat. Phenom. 50 (1990) 159-166

[39] J. Okal, W. Tylus, L. Kepinski, XPS study of oxidation of rhenium metal on γ-Al_2O_3 support, J. Catal. 225 (2004) 498-509

[40] J.F. Watts, J. Wolstenholme, An introduction to surface analysis by XPS and AES. England: John Wiley & Sons, Ltd., (2003) 149-157

[41] B.A. Sexton, N.R. Avery, Coordination of acetonitrile (CH_3CN) to platinum (111): Evidence for an η^2(C, N) species, Surf. Sci. 129 (1983) 21-36

[42] Z. Wu, D. Wang, A. Sun, Surfactant-assisted fabrication of MoS_2 nanospheres, J. Mater. Sci. 45 (2010) 182-187

[43] T. Ungar, Industrial applications of X-ray Diffraction, New York: M. Dekker, Chung & Smith (2000) 847

[44] F.D. Hardcastle, I.E. Wachs, J.A. Horsley, G.H. Via, The structure of surface rhenium oxide on alumina from laser Raman spectroscopy and X-ray absorption Near-edge spectroscopy, J. Mol. Catal. 46 (1988) 15-36

[45] P.L. Gassman, J.S. McCloy, C.Z. Soderquist, M.J. Schweiger, Raman analysis of perrhenate and pertechnetate in alkali salts and borosilicate glasses, J. Raman Spectrosc. 45 (2014) 139-147

[46] O.E. Jaroudi, E. Picquenard, N. Gobeltz, A. Demortier, J. Corset, Raman spectroscopy study of the reaction between sodium sulfide or disulfide and sulfur: Identity of the species formed in solid and liquid phases, Inorg. Chem. 38 (1999) 2917-2923

[47] A. McCreary, J.R. Simpson, Y. Wang, D. Rhodes, K. Fujisawa, L. Balicas, M. Dubey, V.H. Crespi, M. Terrones, A.R. Hight-Walker, Intricate resonant Raman response in anisotropic ReS_2, Nano Lett. 17 (2017) 5897-907

[48] M.G. Stachiotti, F. Cora, C.R.A. Catlow, C.O. Rodriguez, First-principles investigation of ReO_3 sand related oxides. Phys. Rev. B 55 (1997) 7508-7514

[49] J. Purans, A. Kuzmin, E. Cazzanelli, G. Mariotto, Disorder-induced Raman scattering in rhenium trioxide (ReO_3), J. Phys.: Condens. Matter. 19 (2007) 226206

[50] L. Wang, W.K. Hall, The preparation and properties of rhenia-alumina catalysts, J. Catal. 82 (1983) 177-184

[51] E. Cazzanelli, M. Castriota, S. Marino, N. Scaramuzza, J. Purans, A. Kuzmin, R. Kalendarev, G. Mariotto, G. Das, Characterization of rhenium oxide films and their application to liquid crystal cells, J. Appl. Phys. 105 (2009) 114904

[52] C. Castiglioni, F. Negri, M. Rigolio and G. Zerbi, Raman activation in disordered graphites of the A'_1 symmetry forbidden $k\neq0$ phonon: The origin of the D line, J. Chem. Phys. 115 (2001) 3769- 3778

[53] F. Tuinstra, J.L. Koenig, Raman spectrum of graphite, J. Chem. Phys. 53 (1970) 1126-1134

[54] A. Jorio, M.S. Dresselhaus, R. Saito, G. Dresselhaus, Raman spectroscopy in graphene related system, 1st ed Weinheim: Wiley (2011)

[55] A.C. Ferrari, J. Robertson, Interpretation of Raman spectra of disordered and amorphous carbon, Phys. Rev. B 61 (2000) 14095

[56] Y. Feng, *et al.,* Raman vibrational spectra of bulk to monolayer ReS_2 with lower symmetry, Phys. Rev. B 92 (2015) 054110

[57] K. Nakamoto, Infrared and Raman Spectra of Inorganic and Coordination Compounds, in: J.M. Chalmers, P.R. Griffiths, Handbook of Vibrational Spectroscopy, Vol 3, Chichester: John Wiley & Sons (2002) 1872-1892

[58] B.H. Stuart, Infrared Spectroscopy: Fundamentals and Applications. 1st ed England: John Wiley & Sons, 2004

[59] E.S. Zhukova, *et al.,* Vibrational states of a water molecule in a nano-cavity of beryl crystal lattice, J. Chem. Phys. 140 (2014) 224317

[60] C.N.R Rao, R. Venkatarghavan, T.R. Kasturi, Contribution to the infrared spectra of organosulphur compounds, Can. J. Chem. 42 (1964) 36-42

[61] P.A. Shcheglov, D.V. Drobot, Heterogeneous equilibria in the rhenium-oxygen system, Russ. J. Phys. Chem. 80 (2006) 1819-1825

[62] C.A. Majid, M.A. Hussain, Structural transformations in polycrystalline rhenium trioxide, J. Phys. Chem. Solids. 56 (1995) 255-259

[63] S. Eigler, C. Dotzer, F. Hof, W. Bauer, A. Hirsch, Sulfur species in graphene oxide, Chem. Eur. J. 19 (2013) 9490-9496

[64] M.T. Greiner, T.C.R. Rocha, B. Johnson, A. Klyushin, A. Knop-Gericke, R. Schlögl, The oxidation of rhenium and identification of rhenium oxides during catalytic partial oxidation of ethylene: An in-situ XPS study, Phys. Chem. 228 (2014) 521-541

[65] L.O. Chua, Memristor - the missing circuit element, IEEE Trans. Circuit Theory 18 (1971) 507-519

[66] L.O. Chua, S.M. Kang, Memristive devices and systems, Proc. IEEE 64 (1976) 209-223

[67] L.O. Chua, Resistance switching memories are memristors, Appl. Phys. A 102 (2011) 765-783

[68] I. Valov, *et al.,* Nanobatteries in redox-based resistive switches require extension of memristor theory, Nat. Commun. 4 (2013) 1771-9

[69] D.F. Baes, R.E. Mesmer, The hydrolysis of cations, New York: Wiley-Interscience (1979) 193

[70] L. Lange, W. Triebel, Sulfides, polysulfides, and sulfanes, Ullman's Encyclopedia of Industrial Chemistry, Vol 34, Weinheim: Wiley (2000) 659-673

[71] M.A. Vuurman, I. Wachs, In situ Raman spectroscopy of alumina-supported metal oxide catalysts, J. Phys. Chem. 96 (1992) 5008-5016

[72] W. Xue, X.H. Xu, G. Liu, Solid-State Electrochemical Process and Performance Optimization of Memristive Materials and Devices, Chemistry 1 (2019) 44-68

[73] M. Liu, J. Borowiec, L.J.J. Sun, M. Konop, M.M. Rahman, A. Taallah, F.S. Boi, W.P. Gillin, Experimental studies on the conduction mechanism and electrical properties of the inverted Ba doped ZnO nanoparticles based memristor, Appl. Phys. Lett. 115 (2019) 073505

[74] K. Tsunoda, Y. Fukuzumi, J.R. Jameson, Z. Wang, P.B. Griffin, Y. Nishi, Bipolar resistive switching in polycrystalline TiO_2 films, Appl. Phys. Lett. 90 (2007) 113501

[75] R. Xu, H. Jang, M.H. Lee, D. Amanov, Y. Cho, H. Kim, S. Park, H. Shin, D. Ham, Vertical MoS_2 Double-Layer Memristor with Electrochemical Metallization as an Atomic-Scale Synapse with Switching Thresholds Approaching 100 mV, Nano Lett. 19 (2019) 2411-2417

[76] M. Krems, Y.V. Pershin, M. Di Ventra, Ionic Memcapacitive Effects in Nanopores, Nano Letters 10 (2010) 2674-2678

[77] J. Martinez-Rincon, M. Di Ventra and Y.V. Pershin, Solid state memcapacitive system with negative and diverging capacitance, Phys. Rev. B 81 (2010) 195430